JOURNAL OF SYNCHROTRON RADIATION
ISSN 1600-5775

Focusing performance of a multilayer Laue lens with layer placement error described by dynamical diffraction theory

Lingfei Hu, Guangcai Chang, Peng Liu and Liang Zhou*

Beijing Synchrotron Radiation Facility, Institute of High Energy Physics, Chinese Academy of Sciences, 19B Yuquan Road, Shijingshan District, Beijing, People's Republic of China. *Correspondence e-mail: zhouliang@ihep.ac.cn

Received 8 November 2014
Accepted 31 March 2015

Edited by A. Momose, Tohoku University, Japan

Keywords: multilayer Laue lens; dynamical diffraction theory; layer placement error.

The multilayer Laue lens (MLL) is essentially a linear zone plate with large aspect ratio, which can theoretically focus hard X-rays to well below 1 nm with high efficiency when ideal structures are used. However, the focusing performance of a MLL depends heavily on the quality of the layers, especially the layer placement error which always exists in real MLLs. Here, a dynamical modeling approach, based on the coupled wave theory, is proposed to study the focusing performance of a MLL with layer placement error. The result of simulation shows that this method can be applied to various forms of layer placement error.

1. Introduction

Hard X-ray microscopy has wide applications in many areas of science such as life science, materials science, environmental science and so on. Its spatial resolution depends mainly on the numerical aperture of the focused beam. Up to now, various types of X-ray focusing optics utilizing diffraction, reflection and refraction have pushed the spatial resolution to a few tens of nanometers (Schroer & Lengeler, 2005; Kang *et al.*, 2006, 2008; Mimura *et al.*, 2007, 2009; Yan *et al.*, 2011; Koyama *et al.*, 2011; Braun *et al.*, 2013; Huang *et al.*, 2013). Theoretical studies indicate that all of these types of focusing optics, such as the adiabatic refractive lens (Schroer & Lengeler, 2005), multilayer mirror (Mimura *et al.*, 2009), zone plate and multilayer Laue lens (MLL) (Kang *et al.*, 2006; Yan *et al.*, 2007*a*), can focus hard X-rays to well below 10 nm. Among these focusing optical elements, the MLL, a diffractive one, is the most promising to deliver the true nanometer focus (Yan *et al.*, 2007*a*, 2010). The MLL is fabricated by multilayer deposition onto a flat substrate followed by sectioning and thinning (Liu *et al.*, 2005; Kang *et al.*, 2007), whose layers thickness obeys the zone plate law

$$x_n^2 = n\lambda f + n^2\lambda^2/4, \qquad (1)$$

where x_n is the position of the nth layer interface, λ is the wavelength and f is the focal length; the second term in equation (1) can be omitted when $x_n \ll f$. Because of the large aspect ratio, the MLL can be treated as a series of local volume gratings. The geometrical theory becomes invalid and the dynamical diffraction theory, mainly including the coupled wave theory (CWT) (Maser & Schmahl, 1992) and the Takagi–Taupin description (TTD) of dynamical diffraction for volume diffractive optics (Yan *et al.*, 2007*a*), will be used to describe the diffraction properties of the MLL. Currently, the MLL has shown the highest one-dimensional spatial resolution of 11 nm (Huang *et al.*, 2013) and two-dimensional resolution of 25 nm

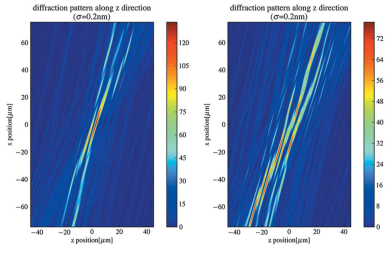

× 27 nm (Yan *et al.*, 2011). Theoretical calculations indicate that the spatial resolution of flat MLLs and wedged MLLs can be further improved to below 10 nm and 1 nm, respectively, when ideal structures without imperfections are used. However, there are different kinds of errors in the MLL during deposition, such as the interface roughness, interface diffusion, layer placement error and so on. The interface roughness and interface diffusion have been studied by CWT (Schneider, 1998) and TTD (Yan, 2009), usually resulting in a reduction of the diffraction efficiency, but have little effect on the resolution. The layer placement error is one of the most serious errors introduced by deposition. A little change in thickness of each layer may result in a significant deviation of the structure from the zone plate law, which can cause phase errors and distort the shape of the intensity profile on the focal plane. Therefore, to reach diffraction-limited focusing, it is important to understand the effect of the layer placement error on the MLL's focusing performance.

The layer placement error can be divided into three forms. In the first form, the interface of each layer deviates from its nominal position by a random error which follows a uniform distribution. This is the simplest way to model the layer placement error but may not be consistent with the deposition. In addition, there is no correlation between interfaces. This form of error is similar to the zone placement error in zone plates, which has been studied by geometrical theory (Simpson & Michette, 1983). For the MLL, it is necessary to study the effect on focusing performance by dynamical diffraction theory. In the second form, the thickness of each layer deviates from their nominal thickness by a random error which follows a Gaussian normal distribution with standard deviation σ and zero mean value. This is different from the first form. The deviation of an interface from its nominal position is the accumulation of thickness errors of all preceding layers, which is similar to the random walk problem. The above two forms can be considered as the high-frequency errors. In the third form, because of the drift of the deposition rate, the spatial frequency of the structure no longer follows a linear relationship with the position of layer x_n but a second- or higher-order polynomial (Yan *et al.*, 2007*b*); this form of the layer placement error can be considered as the low-frequency error.

Among the three forms of layer placement error, the low-frequency error, the third form of the layer placement error, has been studied by TTD (Yan *et al.*, 2007*b*). It is shown that the low-frequency error can result in significant broadening of the focus. However, for the high-frequency errors, the first and second form of the layer placement error, the TTD becomes difficult to apply, for there is no obvious function which can describe these errors. Another effective method which can deal with the high-frequency errors is the beam propagation method (BPM) (Van Roey *et al.*, 1981). This method has been widely used to study the performance of various optical elements such as kinoform (Yan, 2010). However, it lacks real physical interpretation and has the limitation of a paraxial approximation and small numerical aperture (NA). From the result of the BPM, one cannot see the picture of the dynamical diffraction process in the MLL.

In this paper, based on the CWT, we propose a new dynamical modeling approach to study the focusing performance of the MLL with layer placement error. In the following sections, first we describe our method in detail. Then we apply it to low- and high-frequency layer placement errors, and compare the simulation results with TTD and BPM, respectively. Finally we discuss the physical interpretation of high-frequency error effects on focusing performance. It is shown that our method can not only be applied to various forms of layer placement error but can also give a clear physical interpretation.

2. Theory

According to the zone plate law, the thickness of the nth layer is approximately equal to

$$\Delta x_n = x_n - x_{n-1} \approx \lambda f/2x_n \tag{2}$$

which changes slowly with the position of the layer, especially when the layer number n is large. For this reason, the CWT has assumed that the MLL can be divided into a series of small areas; each small area can be considered as a local grating whose grating constant Λ is equal to the average d spacing in this area, $d = x_n - x_{n-2}$, and the diffraction property of the area is the same as an infinite grating with the same grating constant Λ (Schneider, 1997, 1998; Maser & Schmahl, 1992).

However, there is always a small difference among the d spacings in the small area; therefore, the diffraction properties of the layers at different positions in this small area should also be slightly different from each other. Based on this, we further assume that the MLL is composed of a series of local gratings; each local grating consists of only two adjacent layers and its diffraction property is the same as an infinite grating whose grating constant Λ is equal to the thickness of two adjacent layers, $\Lambda = x_n - x_{n-2}$. With this assumption, the effects of the layer placement error on the focusing performance can be easily analyzed when the layer placement error is not too large and the local periodicity is not obviously broken.

From Maxwell equations, the electric field variation of a monochromatic X-ray wave in an infinite grating can be described by the scalar wave equation

$$\nabla^2\mathbf{E}(\mathbf{r}) + k^2[1 + \chi(\mathbf{r})]\mathbf{E}(\mathbf{r}) = 0 \tag{3}$$

where $\mathbf{E}(\mathbf{r})$ is the electric field vector, $k = 2\pi/\lambda$ and $\chi(\mathbf{r})$ is the susceptibility function of the grating. When a plane wave with wavevector $\boldsymbol{\rho}_0$ impinges on the grating, a series of diffracted waves would be excited by the incident wave; their relationships can be expressed as

$$\boldsymbol{\rho}_h = \boldsymbol{\rho}_0 + h\mathbf{G}, \tag{4}$$

where $\boldsymbol{\rho}_h$ is the wavevector of the hth-order diffracted wave, $\mathbf{G}$ is the grating vector, $\mathbf{G} = (2\pi/\Lambda)\mathbf{e}_x$, $\mathbf{e}_x$ is a unit vector perpendicular to the lattice planes. Thus, like the Bloch wavefunction in periodic structures, we can assume that a trial solution to the electric field $\mathbf{E}(\mathbf{r})$ in the grating can be written as the sum of the incident wave and all the diffracted waves,

$$\mathbf{E}(\mathbf{r}) = \sum_{h=-\infty}^{\infty} \mathbf{E}_h(\mathbf{r}) \exp(i\boldsymbol{\rho}_h \cdot \mathbf{r}) = \sum_{h=-\infty}^{\infty} \mathbf{E}_h(\mathbf{r}) \exp\left[i(\boldsymbol{\rho}_0 \cdot \mathbf{r} + h\mathbf{G} \cdot \mathbf{r})\right], \quad (5)$$

where $\mathbf{E}_h(\mathbf{r})$ is the complex amplitude of the hth-order diffracted wave. Because of the periodicity of the grating structures, the susceptibility function $\chi(x)$ can be easily expanded into a Fourier series based on grating vector $\mathbf{G}$,

$$\chi(x) = \sum_{h=-\infty}^{\infty} \chi_h \exp[i\varphi_h(x)] = \sum_{h=-\infty}^{\infty} \chi_h \exp(i2\pi hx/\Lambda) = \sum_{h=-\infty}^{\infty} \chi_h \exp(ih\mathbf{G} \cdot \mathbf{r}). \quad (6)$$

The coefficient χ_h is given by

$$\chi_h = \frac{1}{\Lambda} \int_{x_{n-2}}^{x_{n-1}} \chi_A \exp(-i2\pi hx/\Lambda)\, dx + \frac{1}{\Lambda} \int_{x_{n-1}}^{x_n} \chi_B(x) \exp(-i2\pi hx/\Lambda)\, dx \quad (7)$$

where x_n is the position of the nth layer interface, χ_A and χ_B are the susceptibility of the $(n-1)$th layer and the nth layer, respectively. We note that the phase function φ_h is equal to $h\mathbf{G}\cdot\mathbf{r}$ in equation (6), so the trial solution in equation (5) can be rewritten as

$$\mathbf{E}(\mathbf{r}) = \sum_{h=-\infty}^{\infty} \mathbf{E}_h(\mathbf{r}) \exp\left[i(\boldsymbol{\rho}_0 \cdot \mathbf{r} + \varphi_h)\right]. \quad (8)$$

Substituting equations (6) and (8) into (3), and neglecting the second-order derivatives on $\mathbf{E}_h(\mathbf{r})$, a set of differential equations can be obtained (Yan, 2009),

$$\frac{2i}{k} \nabla E_h \left(\frac{\boldsymbol{\rho}_0}{|\boldsymbol{\rho}_0|} + \frac{\nabla \varphi_h}{k} \right) + \beta_h(\mathbf{r}) E_h + \sum_l \chi_{h-l} E_l \cos \vartheta_{hl} = 0, \quad h, l = 0, \pm 1, \pm 2, \pm 3, \ldots, \quad (9)$$

where ϑ_{hl} is the angle between the polarization directions of two wave components, $\mathbf{E}_h$ and $\mathbf{E}_l$, $\beta_h(\mathbf{r})$ is the deviation function which quantifies the violation of the Bragg condition,

$$\beta_h(\mathbf{r}) = i \frac{\nabla^2 \varphi_h}{k^2} - 2 \frac{\boldsymbol{\rho}_0}{|\boldsymbol{\rho}_0|} \frac{\nabla \varphi_h}{k} - \left(\frac{\nabla \varphi_h}{k} \right)^2. \quad (10)$$

In the derivation of equation (9), the second-order derivatives on $\mathbf{E}_h(\mathbf{r})$ is neglected, which means that the reflected wave at the boundary to the MLL is neglected, as stated by Yan *et al.* (2007*a*) and like assumptions made in conventional first-order coupled wave theory (Erko *et al.*, 2008). In our situation, the MLL structure has 4 nm outmost layer thickness corresponding to the optimal slant angle of 4.85 mrad (89.72° of the incident angle). Under this condition, it is easy to find out that the reflectivity of the X-rays for tungsten is well below 10^{-9}. Thus, the reflectivity is indeed negligible. Further, we point out that, even for a limiting outmost layer thickness of 1 nm, the slant angle is about 0.025 rad (88.57°of the incident angle) and the corresponding reflectivity is still well below 10^{-9} and is negligible. Therefore, in our situation, it is acceptable to neglect the second derivative of the equations.

In the grating, the complex amplitude only depends on the penetration depth z, $E_h(\mathbf{r}) = E_h(z)$, which means $\partial E_h/\partial x = 0$. According to equation (6), $\nabla\varphi_h = 2\pi h/\Lambda \mathbf{e}_x$. In addition, for simplicity, σ polarization is assumed, corresponding to $\cos\vartheta_{hl} = 1$. Substituting these expressions into (9) and (10), they can be further simplified,

$$\frac{2i\cos\theta}{k} \frac{\partial E_h}{\partial z} + \beta_h E_h + \sum_l \chi_{h-l} E_l = 0, \quad \beta_h = -2\frac{h\lambda \sin\theta}{\Lambda} - \left(\frac{h\lambda}{\Lambda}\right)^2, \quad h, l = 0, \pm 1, \pm 2, \pm 3, \ldots, \quad (11)$$

where θ is the angle of incidence. Equation (11) is essentially the same as the Takagi–Taupin equations for strained single crystals where $E_h(\mathbf{r})$ and $\chi(\mathbf{r})$ depend only on one coordinate (Takagi, 1962).

Using the above equations, the complex amplitude of each two adjacent layers on the exit surface can be easily obtained. Then the diffracted wavefront from the entire MLL structure can be constructed by superposing the complex amplitude of each two adjacent layers. The wavefront of an arbitrary point on the exit surface of the MLL can be expressed as

$$E(x) = \sum_h E_h(x) \exp\left[i\left(\frac{2\pi x \sin\theta}{\lambda} + \frac{2\pi hx}{\Lambda} \right) \right] \quad (12)$$

where x is an arbitrary point on the exit surface of the MLL, $x_{n-2} < x < x_n$, $\Lambda = x_n - x_{n-2}$, $E_h(x)$ is the hth-order complex amplitude of the two adjacent layers, the $(n-1)$th and nth layer. The intensity distribution at any point in the focal plane can be calculated by using the Fresnel–Kirchhoff integral (Born & Wolf, 1999); usually only the −1-order diffracted waves, $E_{-1}(x)\exp[i(2\pi x\sin\theta/\lambda - 2\pi x/\Lambda)]$, are used. Then according to the intensity distribution, the effects of the layer placement error on the focusing performance can be obtained.

The above method is very suitable for the second and third form of the layer placement error. However, for the first form of the layer placement error, because of the relative larger destruction of the local periodicity (see the following section), we cannot directly decompose the MLL into a series of local gratings according to the actual interfaces of the layers. In this form of error, only the interfaces of the layers deviate from the nominal position, while the mass center of each layer does not deviate from the nominal position too much. Thus there will be no accumulated error and the overall structure of the MLL will not deviate from the zone plate law. Therefore, we can treat this form of the layer placement error as a small perturbation, and assume that the MLL can be decomposed

into a series of local gratings according to the nominal positions of the interfaces of the layers, whose grating constant Λ' can be expressed as

$$\Lambda' = x'_n - x'_{n-2}, \tag{13}$$

where x'_n is the nominal position of the interface of the nth layer. Then we can still use the above method to study the effect of the first form of the layer placement error, except that equations (6), (7) and (12) are changed into the following equations, respectively,

$$\chi(x) = \sum_{h=-\infty}^{\infty} \chi_h \exp(i2\pi hx/\Lambda'), \tag{14}$$

$$\chi_h = \frac{1}{\Lambda'} \int_{x'_{n-2}}^{x'_n} \chi(x) \exp(-i2\pi hx/\Lambda')\, \mathrm{d}x, \tag{15}$$

$$E(x) = \sum_h E_h(x) \exp\left[i\left(\frac{2\pi x \sin\theta}{\lambda} + \frac{2\pi hx}{\Lambda'}\right)\right], \tag{16}$$

where $\chi(x)$ in equation (15) is the actual susceptibility of material in position x.

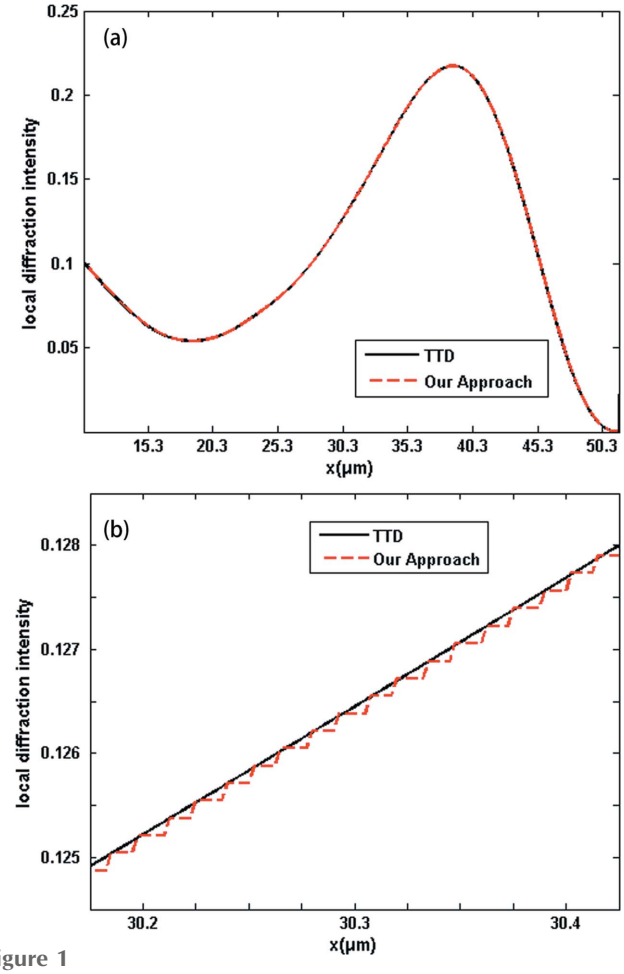

Figure 1
(*a*) The local −1-order diffraction intensity at the exit surface of the MLL. The black line is calculated by the TTD method. The red line is calculated by our approach. (*b*) Enlarged image of local diffraction intensity around x_n = 30.3 μm.

3. Simulation

In order to verify the reliability of our approach, the obtained results are compared with those calculated from the TTD and BPM. Here a flat MLL (WSi_2/Si) with the following parameters is considered: a focal length of 4 mm at 12 keV, an outermost layer thickness of 4 nm and an innermost layer thickness of 20 nm which correspond to a lens aperture size of about 41 μm, a tilted angle of 4.85 mrad and a section depth of 5 μm which are used to reduce the dynamical diffraction effect and achieve a diffraction-limited 10 nm focus.

3.1. Ideal structures

The TTD, BPM and our approach are used to calculate the focusing performance of the MLL with ideal structure. Fig. 1(*a*) shows the −1-order local diffraction intensities calculated by TTD and our approach, Fig. 1(*b*) shows an enlarged image of the region around x_n = 30.3 μm. Due to our assumption, the local diffraction intensity calculated by our approach is a constant over the two adjacent layers. Because of the different sampling points on the exit surface in these three methods, for convenience the obtained intensity profiles on the best focal plane will be compared with each other. Fig. 2 shows the intensity profiles on the best focal plane calculated by TTD, BPM and our approach. To evaluate the difference among the intensity profiles, the R-factor in crystallography is used, which is defined as

$$R = \frac{\sum_n \left| |E'(\Delta x_n)|^2 - |E(\Delta x_n)|^2 \right|}{\sum_n |E'(\Delta x_n)|^2}, \tag{17}$$

where $E(\Delta x_n)$ is the complex amplitude calculated by our approach, $E'(\Delta x_n)$ is the complex amplitude calculated by the TTD or BPM, Δx_n is the nth sampling point on the focal plane. Because most of the intensity is diffracted into a very small region on the best focal plane, only the sampling points where $E'(\Delta x_n) > 0.1E'_{\max}$ are used in equation (17); $E'_{\max}$ is the maximum of $E'(\Delta x_n)$. In crystallography, an R-factor of less

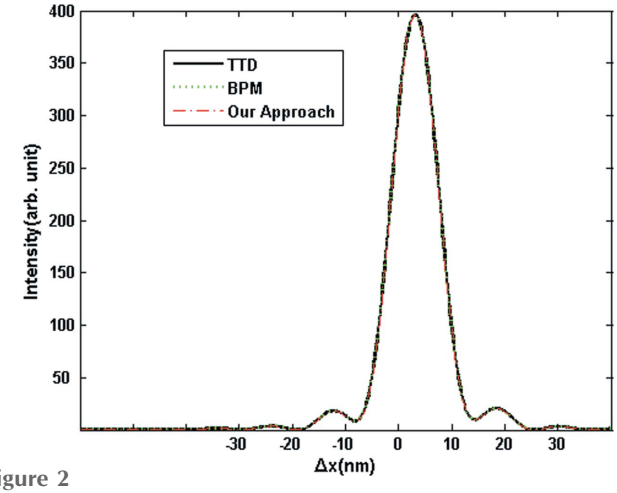

Figure 2
Intensity profiles on the best focal plane calculated by TTD, BPM and our approach.

than 15% usually indicates good agreement between two data sets (Neutze *et al.*, 2000; McRee, 1999; Drenth, 2007). As shown in Figs. 1 and 2, the results obtained by our approach agree very well with those calculated by TTD and BPM. The *R*-factor of the intensity profiles compared with that calculated by TTD and BPM is 0.1% and 0.2%, respectively.

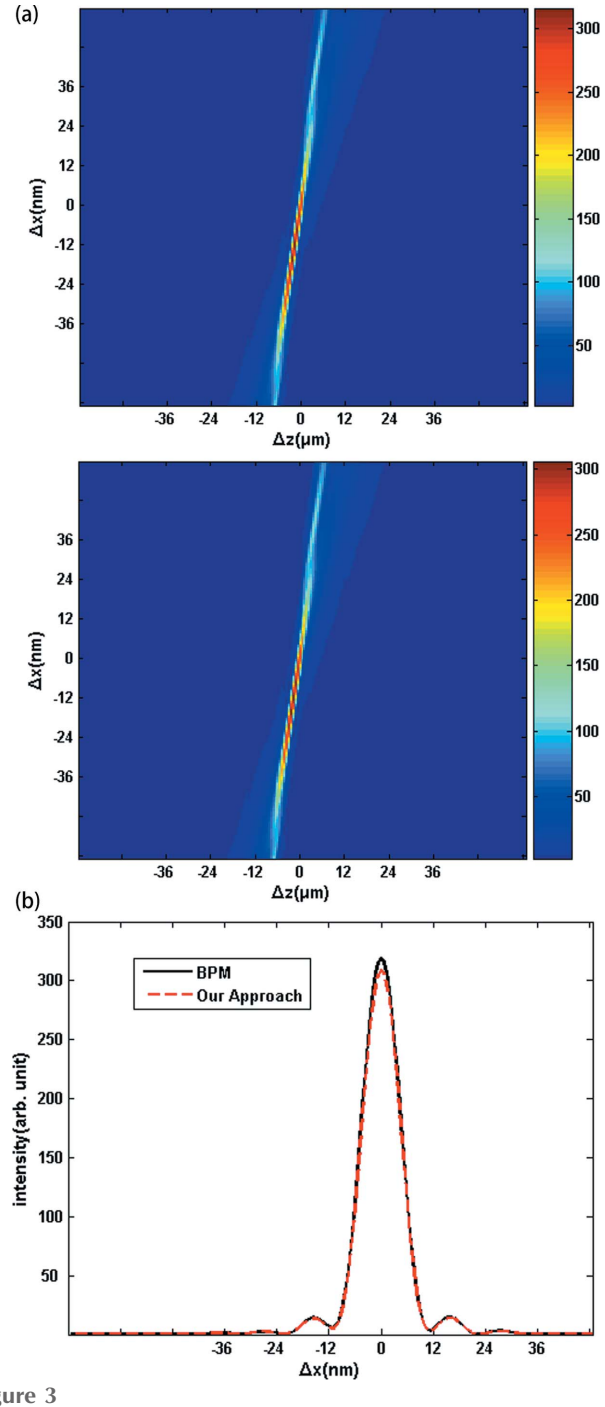

Figure 3
(*a*) Top: the isophotes near the focus calculated by BPM when $\varepsilon = 0.4$, where Δz and Δx are parallel and transverse to the incident beam. Bottom: the isophotes near the focus calculated by our approach when $\varepsilon = 0.4$. (*b*) The intensity profiles on the best focal plane calculated by BPM and our approach when $\varepsilon = 0.4$. The black line is calculated by BPM. The red line is calculated by our approach.

3.2. First form of the layer placement error

Just as the error analysis in zone plate manufacturing (Simpson & Michette, 1983), we assume the first form of error is the independent layer position error. The parameter $\varepsilon = \alpha/\Delta x_n$ is used to characterize the magnitude of the error, where Δx_n is the thickness of the outmost layer, and α indicates that the actual position of layer x_n follows a uniform distribution in $[x_n' - \alpha, x_n' + \alpha]$, x_n' is the nominal position of the layer. This is a relatively simple model and the independent random variable here is the layer position. Each position could be viewed as being independent of each other. This model suggests that during fabrication there is no layer position error stacking which is in contrast with the next section. Figs. 3(*a*) and 3(*b*) show isophotes near the focus and the intensity profiles on the best focal plane calculated by BPM and our approach, respectively, when $\varepsilon = 0.4$. Fig. 4 shows the *R*-factor as a function of ε. It can be observed that the intensity profiles calculated by our approach and the BPM are almost the same even if the magnitude of error is relatively large.

3.3. Second form of the layer placement error

The second form of the layer placement error is assumed to be a Gaussian thickness random error. As mentioned previously, each layer thickness is the addition of the nominal thickness and a random error following a Gaussian distribution which means that each layer thickness is considered to be an independent random variable. Thus, the actual position of each layer is the addition of the nominal position and the accumulated preceding thickness errors.

In the following a statistical description of the Gaussian thickness random error is given. Although the independent random variable in this form is the layer thickness, we are still interested in the layer position. As mentioned above, x_n represents the layer position of the nth layer. Let Δd_n be the thickness error of the nth layer. Then Δd_n is the independent random variable of the Gaussian distribution. $\langle \Delta d_n \rangle = 0$,

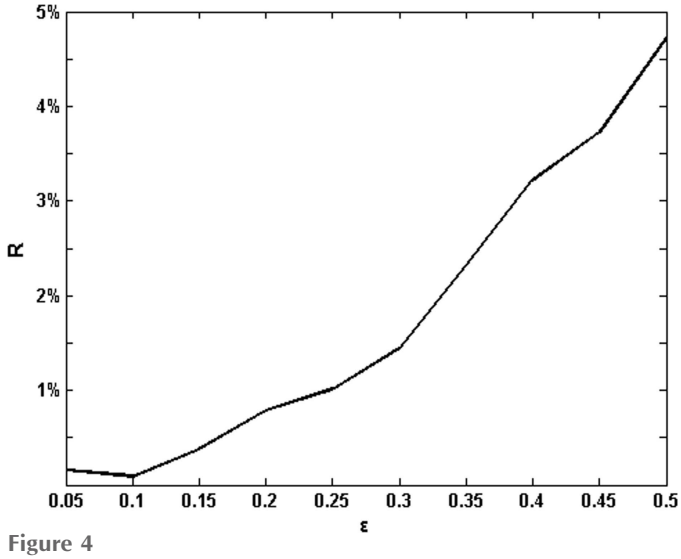

Figure 4
R-factor *versus* the parameter ε. The *R*-factor shows that these two methods are in good agreement with each other.

$\langle \Delta d_n^2 \rangle = \sigma^2$. Here $\langle \ldots \rangle$ represents the mean value. The nth layer position could be calculated as

$$\begin{aligned} x_n &= x_1' + (x_2' - x_1') + \Delta d_1 + (x_3' - x_2') \\ &\quad + \Delta d_2 + \ldots + (x_n' - x_{n-1}') + \Delta d_n \\ &= x_n' + \Delta d_1 + \Delta d_2 + \ldots + \Delta d_n. \end{aligned} \tag{18}$$

x_1' is the initial layer position of the innermost zone; the corresponding layer number is n_0. x_n' still corresponds to the nominal layer position. According to the Δd_n characteristics, we have $\langle \Delta x_n \rangle = 0$ and $\langle \Delta x_n^2 \rangle = n\sigma^2$, where $\Delta x_n = x_n - x_n'$ is the deviation from its nominal position x_n'. Further, the summation of n Gaussian independent variables is also Gaussian and its mean value is 0 and standard deviation σ_n is $n^{1/2}\sigma$. This means that, although the layer position of the $(n + n_0)$th layer has the mean value of its nominal position, its standard deviation is proportional to the square root of its layer number minus the initial layer number. Recall that the MLL structure discussed here is 4 nm to its outmost layer thickness and 20 nm to its innermost layer thickness. The corresponding layer number is about 260 to 6400. The outmost layer error standard deviation could be up to about 80σ. When assuming that the MLL is located at its ideal position, the stacked layer error accumulates with an increase in the layer number. This corresponds to a phase deviation and is discussed in detail in §4. Fig. 5 illustrates that, even at the same σ (σ = 0.2 nm), the final MLL performance could be very different. Due to the tremendous uncertainty of this error, a statistical evaluation of the final performance has to be conducted. The criteria given in §3.4 are obtained through superposition of various figures at the focal plane. Figs. 6(*a*) and 6(*b*) show isophotes near the

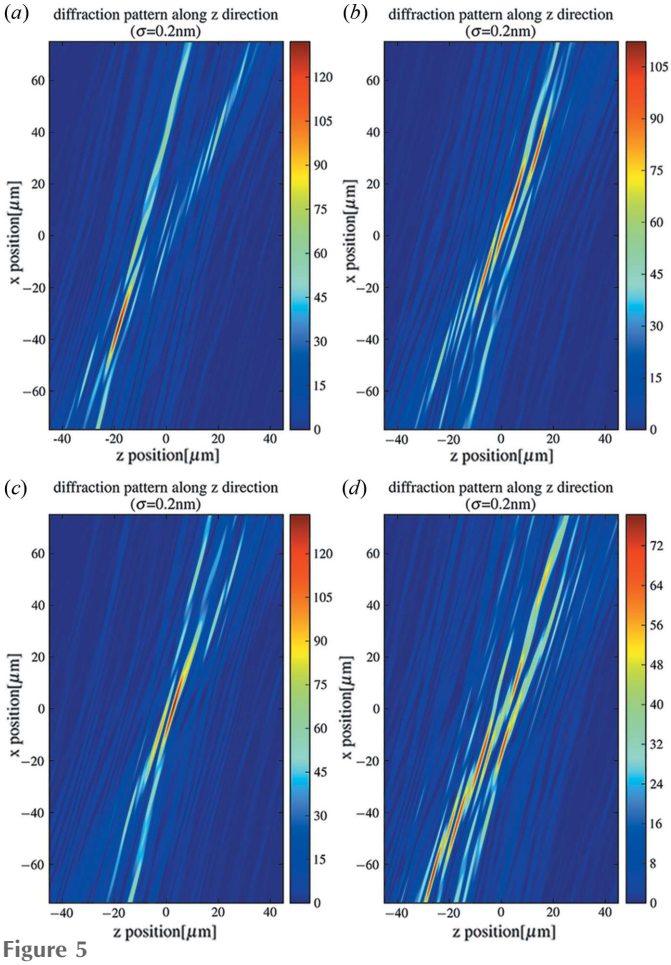

Figure 5
(*a*), (*b*), (*c*), (*d*) are the isophotes near the focus along the propagation direction under the same conditions (σ = 0.2 nm).

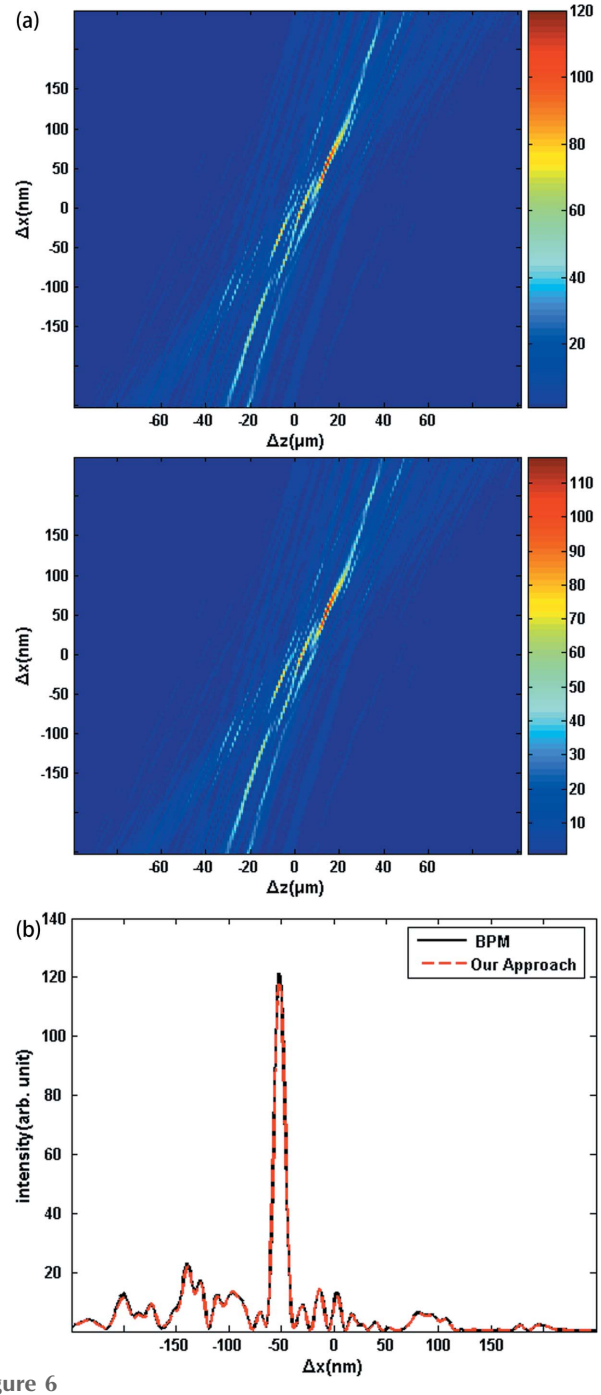

Figure 6
(*a*) Top: the isophotes near the focus calculated by BPM when σ = 0.2 nm, where Δz and Δx are parallel and transverse to the incident beam. Bottom: the isophotes near the focus calculated by our approach when σ = 0.2 nm. (*b*) The intensity profiles on the best focal plane calculated by BPM and our approach when σ = 0.2 nm. The black line is calculated by BPM. The red line is calculated by our approach.

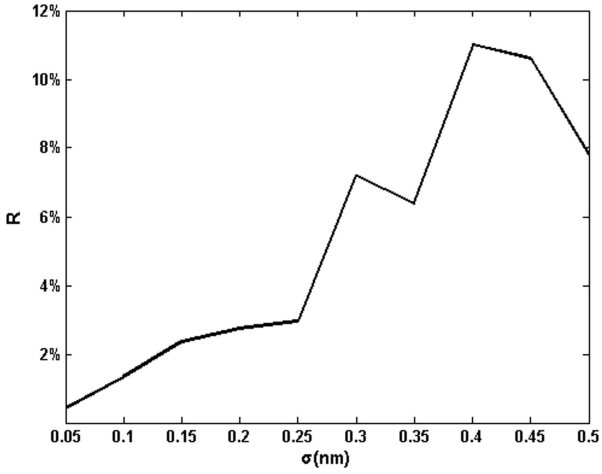

Figure 7
R-factor *versus* the standard deviation σ. The *R*-factor shows that these two methods are in good agreement with each other

focus and intensity profiles on the best focal plane calculated by BPM and our approach when $\sigma = 0.2$ nm, where σ is the standard deviation of the Gaussian normal distribution. Fig. 7 shows the *R*-factor as a function of σ. It can be observed that the intensity profiles calculated by our approach and the BPM are almost the same even if $\sigma = 0.5$ nm.

3.4. Third form of the layer placement error

For the third form of the layer placement error, the spatial frequency of the structure $1/d$ can be express as a second- or higher-order polynomial (Yan *et al.*, 2007*b*). Fig. 8(*a*) shows the intensity isophote patterns calculated near the focus by TTD and our approach when $1/d = -0.023x_n^2 + 5.7x_n - 8.7$; Fig. 8(*b*) shows the intensity profiles on the best focal plane. The *R*-factor of the intensity profile compared with that calculated by TTD is 0.34%, which means that these two methods are in good agreement with each other.

3.5. Strehl ratio for the high-frequency error

Further, Figs. 9(*a*) and 9(*b*) show the Strehl ratio, defined as the ratio of the peak intensity in the best focal plane of the MLL with the layer placement error to that of the MLL with ideal structure (Born & Wolf, 1999), for the first and the second layer placement error, respectively. Fig. 9(*a*) indicates that in the first form of the layer placement error situation, without correlation between each layer, the Strehl ratio stays relatively high even to large ε. In contrast, Fig. 9(*b*) shows that in the second form of the layer placement error situation, the Strehl ratio drops quickly as σ increases. Note that in Fig. 8(*b*), $\sigma > 0.05$ nm leads to a dramatically decrease of the Strehl ratio. By convention, for the diffraction limit, the Strehl limit is set to 0.8. This gives accuracy requirements of about $\varepsilon \leq 0.4$ and $\sigma \leq 0.05$ nm, respectively.

The intensity profiles at the best focal plane for different parameters are also given in Figs. 10(*a*) and 10(*b*). For comparison, the peaks are shifted to the same position. These figures again illustrate the peak intensity variation with the

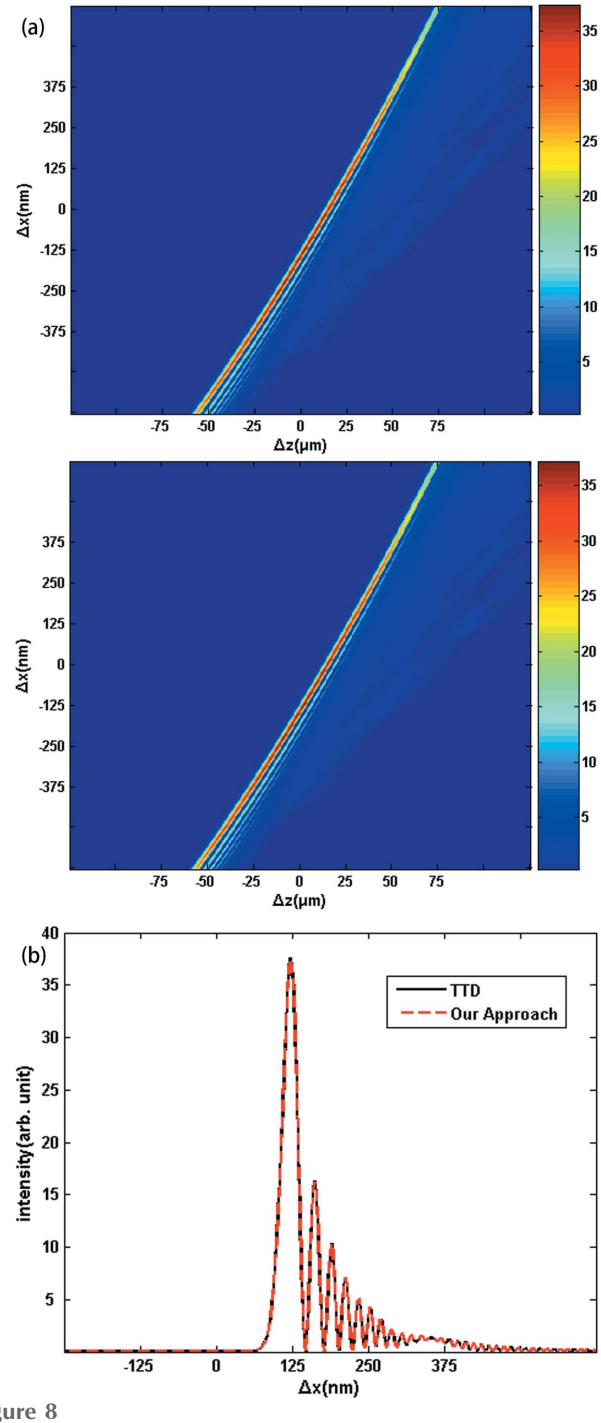

Figure 8
(*a*) Top: the isophotes near the focus calculated by TTD when $1/d = -0.023x_n^2 + 5.7x_n - 8.7$, where Δz and Δx are parallel and transverse to the incident beam. Bottom: the isophotes near the focus calculated by our approach when $1/d = -0.023x_n^2 + 5.7x_n - 8.7$. (*b*) The intensity profiles on the best focal plane calculated by TTD and our approach when $1/d = -0.023x_n^2 + 5.7x_n - 8.7$. From the figure, we can see that our approach and TTD yield exactly the same result.

parameters ε and σ changing. For the first form of the MLL layer placement, even to $\varepsilon = 0.4$, which corresponds to the uniform deviation of the layer position between −1.6 nm and 1.6 nm, the diffraction pattern is conserved to some extent. In contrast, for the second form of the MLL layer placement, $\sigma =$

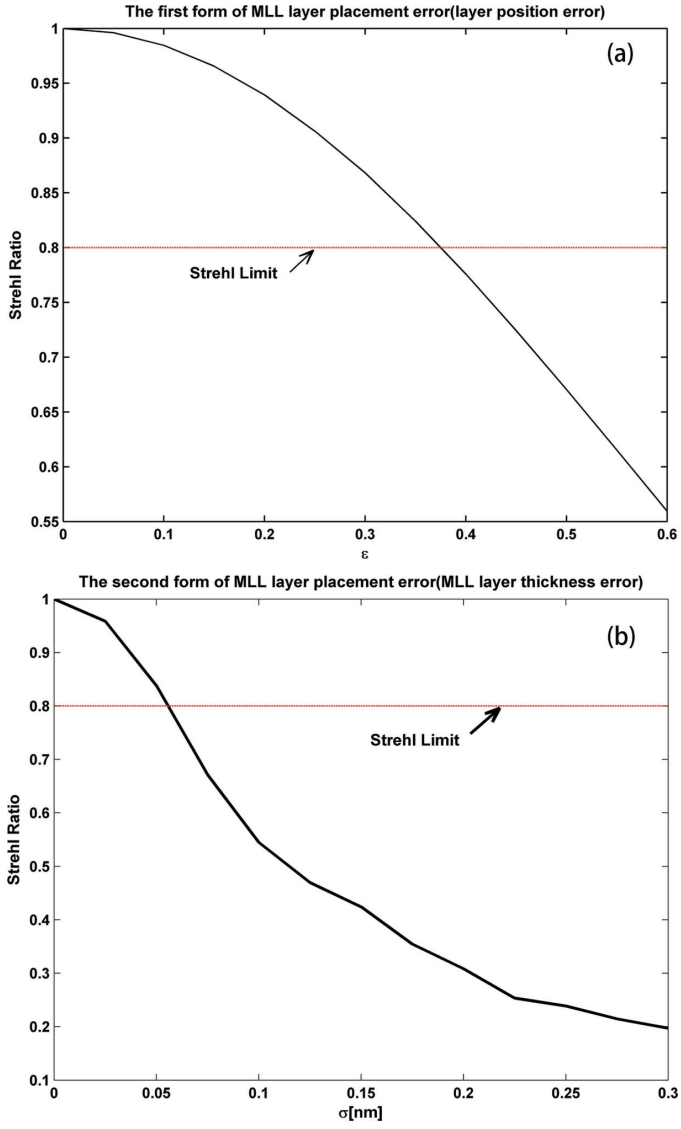

Figure 9
(*a*) The Strehl ratio decreases as ε increases. ε is defined to characterize the magnitude of the first form of the error. (*b*) The Strehl ratio decreases as σ increases. σ is the standard deviation of the Gaussian normal distribution. The red line sets the Strehl limit to 0.8.

0.1 nm leads to a drastically decreasing maximum intensity while generating strong side peaks.

4. Discussion

From the simulation results shown in the previous sections, one observes that for the first form of the layer placement error the main effect is the decrease in peak intensity while keeping the focus size. The second form of the layer placement error would result in the reduction of the peak intensities and generation of very strong side peaks, thereby destroying the focus. The third form of the layer placement error, which leads to significant broadening of the focus and apparent redundant fringes, has been discussed elsewhere (Yan *et al.*, 2007*b*). This section only focuses on the two high-frequency errors.

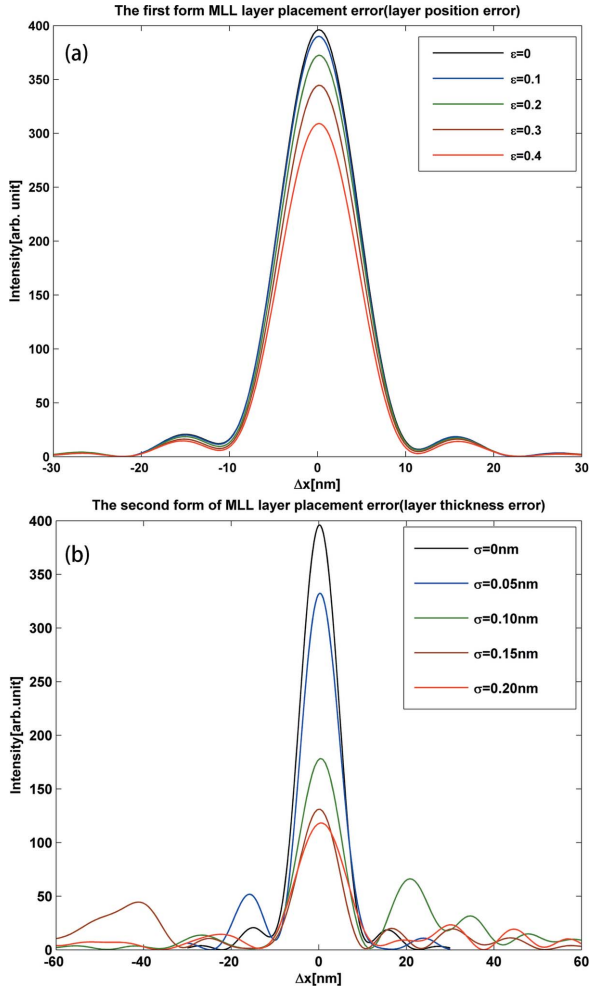

Figure 10
(*a*) Intensity profiles on the best focal plane at different ε. (*b*) Intensity profiles on the best focal plane at different σ.

The intensity distribution near the −1-order focus is generated by the propagation of the −1-order diffracted wave, $E_{-1}(\mathbf{r})\exp[i(\boldsymbol{\rho}_0\cdot\mathbf{r} + \varphi_{-1})]$. Figs. 11(*a*) and 11(*b*) give the phase deviation of the −1-order diffracted wave with the two high-frequency placement errors from a perfect converging spherical wave at the exit surface of the MLL. Also, the phase deviation of the MLL with ideal structures is plotted as a comparison. Compared with these two figures, it shows that the first form of the error conserves the phase relations to some extent, while the second form of the error violates the phase relations drastically and the phase deviation varies rapidly over π radians in most regions. That means, in the first form of the placement error situation, the destruction of focusing is not severe compared with the ideal MLL, which has been stated in the previous section. On the other hand, from Figs. 6(*a*) and 6(*b*) one can easily see the destruction of focusing in the second form of the layer placement error situation. This corresponds to the phase deviation of the −1-order diffracted wave at the exit surface of the MLL in Fig. 11(*b*).

Figs. 12(*a*) and 12(*b*) further show the phase errors of the −1-order diffracted wave calculated by two independent

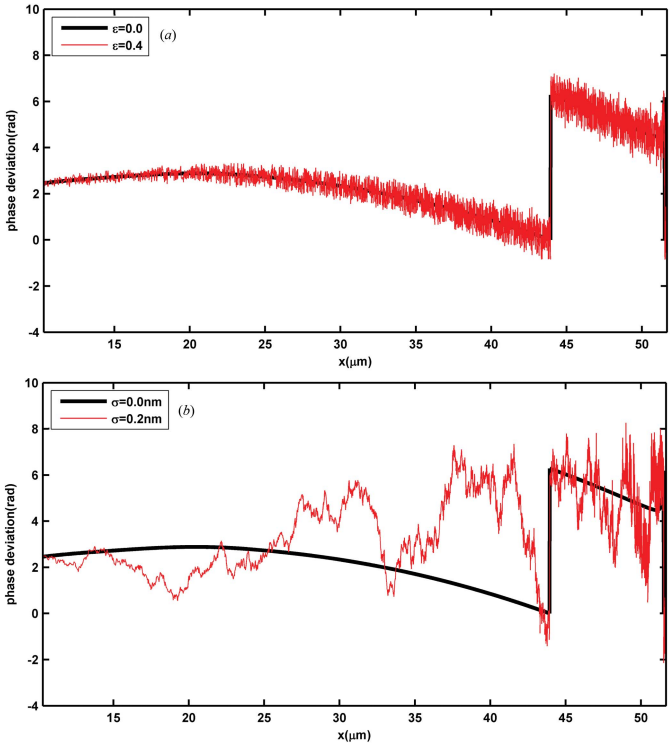

Figure 11
(*a*) Phase deviations of the −1-order diffracted wave with the first form of the layer placement error and ideal structures from a perfect converging spherical wave at the exit surface of the MLL. The black line corresponds to the ideal structures and the red line corresponds to the situation $\varepsilon = 0.4$. (*b*) Phase deviations of the −1-order diffracted wave with the second form of the layer placement error and ideal structures from a perfect converging spherical wave. The black line corresponds to the ideal structures and the red line correspond to the situation $\sigma = 0.2$ nm.

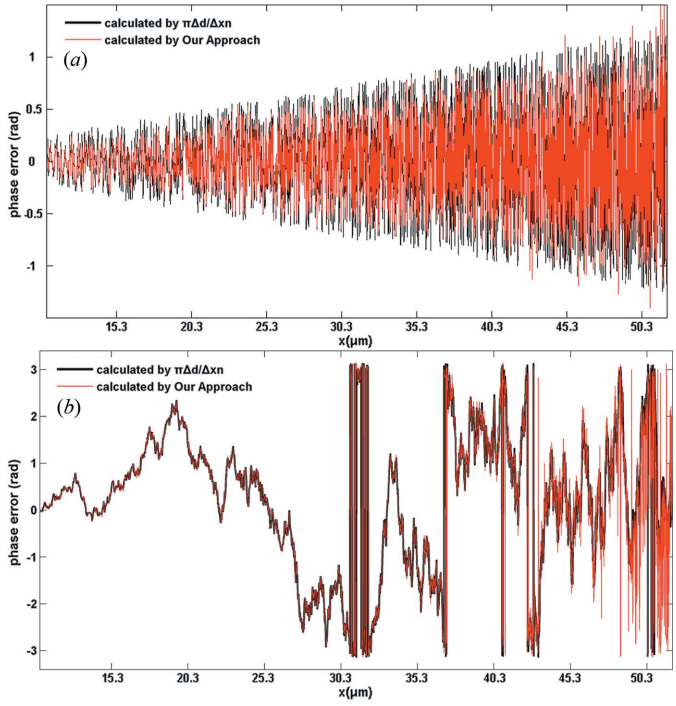

Figure 12
(*a*) Phase errors of the −1-order diffracted wave with the first form of the layer placement error, $\varepsilon = 0.4$. (*b*) Phase errors of the −1-order diffracted wave with the second form of the layer placement error, $\sigma = 0.2$ nm. The black line is the result obtained from the analytical expression $\pi\Delta d/\Delta x_n$. The red line is obtained by calculating the phase difference between two −1-order diffracted waves, one with the layer placement error and the other with the ideal structure. Note that the phase deviation is presented as mod 2π in this figure in contrast to previous figures.

methods. The phase error deviation from ideal structures can be directly calculated by the actual layer position and equals $\pi\Delta d/\Delta x_n$, where Δd is the displacement of the nth layer and Δx_n is the nominal thickness of the nth layer (Huang *et al.*, 2013). The phase error can also be obtained by calculating the phase difference between two −1-order diffracted waves, one with the layer placement error and the other with the ideal structure. As shown in Fig. 12, these two independent phase error calculations agree with each other. Thus this indicates that the phase deviation of the diffracted wave is caused by the layer placement error. Knowing this, we can further explain the different effects of the two forms of layer placement error on focusing performance. According to this assumption, the first form of the layer placement error considers the layer positions while the second form of the layer placement error considers the layer thickness to be the independent random variables. In the first form of the layer placement error, there is no correlation between interfaces, while in the second form the interface is the accumulation of all preceding layer thicknesses, which could lead to a vast deviation of the actual positions of the layers from the nominal positions in most regions of the MLL. The accumulated errors lead to an obvious destruction of focusing.

5. Conclusion

From basic Maxwell equations, based on the CWT and some new assumptions, we derive a dynamical modeling approach to calculate the focusing performance of the MLL with ideal structures and layer placement errors. This means that for a MLL with ideal structures or the second or third form of the layer placement error, the MLL could be seen as a series of local gratings, each of which consists of only two adjacent layers, when the local periodicity is not obviously broken; for the MLL with the first form of the layer placement error, the error can be seen as a small perturbation. Agreement with the TTD method shows the validity of our approach. Then we extend our approach to three forms of the layer placement error and analyze the effects of these errors on the focusing performance. Agreement with the BPM method in high-frequency errors and the TTD method in low-frequency error shows that our method could be used in various situations. Apart from that, from the deduction of the theory, our approach shows a more physical meaning than simple numerical methods like BPM. Also we discuss the physical interpretation of the effects of the two forms of high-frequency error on the focusing performance. We point out that the phase deviation of the diffracted wave is caused by the layer placement error. Due to the accumulation of all

preceding layer errors, the second form of the layer displacement error, the layer thickness error, affects the focusing performance a lot while the first form of the layer placement error, the layer position error, has less effect. We believe that our approach can help in analyzing the effect of the layer placement error on the focusing performance, obtaining intolerable levels of layer placement error and depositing a more accurate MLL.

Acknowledgements

We thank Hanfei Yan at Brookhaven National Laboratory for help of the classification of the layer placement error and the TTD theory. This work was supported by Project 11305201 supported by NSFC.

References

Born, M. & Wolf, E. (1999). *Principles of Optics: Electromagnetic Theory of Propagation, Interference and Diffraction of Light.* CUP Archive.

Braun, S., Kubec, A., Menzel, M., Niese, S., Krüger, P., Seiboth, F., Patommel, J. & Schroer, C. (2013). *J. Phys. Conf. Ser.* **425**, 052019.

Drenth, J. (2007). *Principles of Protein X-ray Crystallography*. New York: Springer.

Erko, A. I., Idir, M., Krist, T. & Michette, A. G. (2008). *Modern Developments in X-ray and Neutron Optics.* Berlin: Springer.

Huang, X., Yan, H., Nazaretski, E., Conley, R., Bouet, N., Zhou, J., Lauer, K., Li, L., Eom, D., Legnini, D., Harder, R., Robinson, I. K. & Chu, Y. S. (2013). *Sci. Rep.* **3**, 3562.

Kang, H., Maser, J., Stephenson, G., Liu, C., Conley, R., Macrander, A. & Vogt, S. (2006). *Phys. Rev. Lett.* **96**, 127401.

Kang, H. C., Stephenson, G. B., Liu, C., Conley, R., Khachatryan, R., Wieczorek, M., Macrander, A. T., Yan, H., Maser, J., Hiller, J. & Koritala, R. (2007). *Rev. Sci. Instrum.* **78**, 046103.

Kang, H. C., Yan, H., Winarski, R. P., Holt, M. V., Maser, J., Liu, C., Conley, R., Vogt, S., Macrander, A. T. & Stephenson, G. B. (2008). *Appl. Phys. Lett.* **92**, 1114.

Koyama, T., Takenaka, H., Ichimaru, S., Ohchi, T., Tsuji, T., Takano, H. & Kagoshima, Y. (2011). *10th International Conference on X-ray Microscopy*, pp. 24–27. AIP Publishing.

Liu, C., Conley, R., Macrander, A., Maser, J., Kang, H., Zurbuchen, M. & Stephenson, G. (2005). *J. Appl. Phys.* **98**, 113519.

McRee, D. E. (1999). *Practical Protein Crystallography*. New York: Academic Press.

Maser, J. & Schmahl, G. (1992). *Opt. Commun.* **89**, 355–362.

Mimura, H., Handa, S., Kimura, T., Yumoto, H., Yamakawa, D., Yokoyama, H., Matsuyama, S., Inagaki, K., Yamamura, K. & Sano, Y. (2009). *Nat. Phys.* **6**, 122–125.

Mimura, H., Yumoto, H., Matsuyama, S., Sano, Y., Yamamura, K., Mori, Y., Yabashi, M., Nishino, Y., Tamasaku, K. & Ishikawa, T. (2007). *Appl. Phys. Lett.* **90**, 051903.

Neutze, R., Wouts, R., van der Spoel, D., Weckert, E. & Hajdu, J. (2000). *Nature (London)*, **406**, 752–757.

Schneider, G. (1997). *Appl. Phys. Lett.* **71**, 2242–2244.

Schneider, G. (1998). *Appl. Phys. Lett.* **73**, 599–601.

Schroer, C. G. & Lengeler, B. (2005). *Phys. Rev. Lett.* **94**, 054802.

Simpson, M. J. & Michette, A. G. (1983). *Opt. Acta*, **30**, 1455–1462.

Takagi, S. (1962). *Acta Cryst.* **15**, 1311–1312.

Van Roey, J., Van der Donk, J. & Lagasse, P. (1981). *J. Opt. Soc. Am.* **71**, 803–810.

Yan, H. (2009). *Phys. Rev. B*, **79**, 165410.

Yan, H. (2010). *Phys. Rev. B*, **81**, 075402.

Yan, H., Kang, H. C., Conley, R., Liu, C., Macrander, A. T., Stephenson, G. B. & Maser, J. (2010). *X-ray Opt. Instrum.* **2010**, 401854.

Yan, H., Kang, H., Maser, J., Macrander, A., Kewish, C., Liu, C., Conley, R. & Stephenson, G. (2007*b*). *Nucl. Instrum. Methods Phys. Res. A*, **582**, 126–128.

Yan, H., Maser, J., Macrander, A., Shen, Q., Vogt, S., Stephenson, G. B. & Kang, H. C. (2007*a*). *Phys. Rev. B*, **76**, 115438.

Yan, H., Rose, V., Shu, D., Lima, E., Kang, H. C., Conley, R., Liu, C., Jahedi, N., Macrander, A. T. & Stephenson, G. B. (2011). *Opt. Express*, **19**, 15069–15076.